THE JOURNAL OF PHYSICAL CHEMISTRY A

Article

Cite This: J. Phys. Chem. A 2019, 123, 9008−9018

pubs.acs.org/JPCA

Computational Study of the Effect of Mineral Dust on Secondary Organic Aerosol Formation by Accretion Reactions of Closed-Shell Organic Compounds

Fatemeh Keshavarz,*[,†] Anna Shcherbacheva,[†] Jakub Kubečka,[†] Hanna Vehkamäki,[†] and Theo Kurtén[‡]

[†]Institute for Atmospheric and Earth System Research, Faculty of Science and [‡]Department of Chemistry, Faculty of Science, University of Helsinki, Helsinki FI-00014, Finland

Supporting Information

ABSTRACT: The effect of dust aerosols on accretion reactions of water, formaldehyde, and formic acid was studied in the conditions of earth's troposphere at the DLPNO-CCSD(T)/aug-cc-pVTZ//ωB97X-D/6-31++G** level of theory. A detailed analysis of the reaction mechanisms in the gas phase and on the surface of mineral dust, represented by mono- and trisilicic acid, revealed that mineral dust has the potential of decreasing reaction barrier heights. Specifically, at 0 K, mineral dust can lower the apparent energy barrier of the reaction of formaldehyde with formic acid to zero. However, when the entropic contributions to the reaction free energies were accounted for, mineral dust was found to selectively enhance the reaction of water with formaldehyde, while inhibiting the reaction of formaldehyde and formic acid, in the lower parts of the troposphere (with temperatures around 298 K). In the upper troposphere (with temperatures closer to 198 K), mineral dust catalyzes both reactions and also the reaction of methanol with formic acid. Despite the intrinsic potential of mineral dust, calculation of the catalytic enhancement parameter for a likely range of dust aerosol concentrations suggested that dust aerosols will not contribute to secondary organic aerosol formation via dimerization of closed-shell organic compounds. The main reason for this is the relatively low absolute concentration of tropospheric dust aerosol and its inefficiency in increasing the effective reaction rate coefficients.

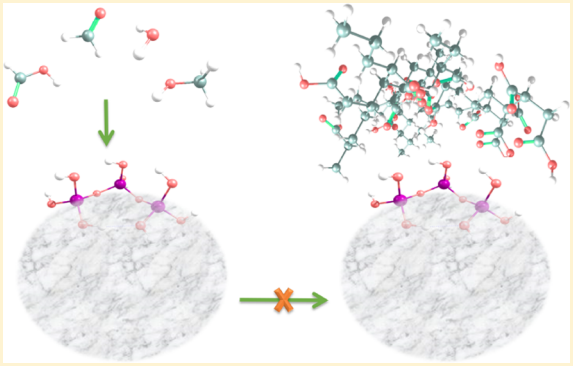

1. INTRODUCTION

Aerosols affect the climate and the quality of human life in many ways. Their impacts include visibility reduction,[1] regulation of precipitation by acting as cloud condensation nuclei,[2] altering biogeochemical cycles,[3] controlling the energy budget of earth through radiative forcing,[3] and imposing adverse health effects[4−6] While the contribution of mineral dust to atmospheric aerosols is noticeable, and mineral dust is emitted to the atmosphere at a high rate, organic materials usually dominate fine atmospheric aerosols.[5,7,8] To be more specific, the total global emission rates of mineral dust particles with the 0.1−1.0 and 0.1−10.0 μm particle sizes are estimated to be 48 and 10 100 Tg yr^{-1}, respectively. In comparison, the global emissions of organic aerosols are about 200 Tg yr^{-1}.[9] Moreover, around 20−60% of the total mass of atmospheric aerosols observed in the continental midlatitudes and up to 90% in tropical forested areas have been found to consist of organic materials.[1] Organic aerosols can be divided into primary organic aerosols (POAs, the organic matter emitted directly from natural and anthropogenic sources) and secondary organic aerosols (SOAs, the organic matter emitted in a gaseous form and transformed to particles in the atmosphere via different reaction paths whether forming entirely new particles or condensing on preexisting particles[10]).[1,7,11] The amount of SOAs exceeds that of POAs even in heavily urbanized areas,[11] and SOAs can form up to 90% of the total organic mass of atmospheric aerosols.[5,12]

Although SOAs and POAs are abundant and display profound impacts on the Earth's climate, their composition has been poorly understood since their chemistry is highly complex[13] and varies with life time,[14] and experimental measurements are bound to large uncertainties[15] due to the difficulty in detecting low volatility compounds with high molecular weights.[16,1] Regardless of the complex chemistry, two general routes have been suggested for SOA formation. The first route is related to gas-phase oxidation of volatile organic compounds by ozone, hydroxyl radical (OH), nitrate radical (NO_3), and other atmospheric oxidants, which leads to both fragmentation (ultimately to CO_2) and production of organic compounds with multiple functional groups. The

Received: July 3, 2019
Revised: September 6, 2019
Published: September 26, 2019

DOI: 10.1021/acs.jpca.9b06331
J. Phys. Chem. A 2019, 123, 9008−9018

polyfunctional products with intermediate or low volatilities may then partition onto preexisting organic aerosols, increasing the SOA mass.[17] The second route occurs in the particle phase. In this route, the gas- and liquid-phase atmospheric oxidants oxidize the organic compounds of aerosols, also leading to an increase in the organic mass.[18] This process is one of the processes involved in aerosol aging.[19] In addition, in the second route, nonoxidative combination of organic compounds can generate high-molecular-weight oligomers.[20,21] Such accretion reactions[22] have attracted much interest since they can produce organic species with much lower saturation vapor pressures compared to the precursor reactants.[23] For example, the following classes of accretion reactions have been experimentally studied with respect to their role in SOA formation[24]

$$\mathrm{ROOH(hydroperoxide) + R'CHO(aldehyde) \rightleftharpoons ROOCHR'OH(peroxyhemiacetal)} \quad \text{(R1)}$$

$$\mathrm{ROH(alcohol) + R'CHO(aldehyde) \rightleftharpoons ROCHR'OH(hemiacetal)} \quad \text{(R2)}$$

$$\mathrm{RCCOR'(carbonyl) + R''COR'''(carbonyl) \rightleftharpoons CR''R'''OHCRCR'O(aldol\ addition\ product)} \quad \text{(R3)}$$

$$\mathrm{RCO_2H(carboxylic\ acid) + R'OH(alcohol\ or\ carboxylic\ acid) \rightleftharpoons RCOR'O(ester\ or\ acid\ anhydride) + H_2O} \quad \text{(R4)}$$

$$\mathrm{SO_2(OH)_2(sulfuric\ acid) + ROH(alcohol\ or\ gem-diol) \rightleftharpoons SO_2(OH)(OR)(sulfate\ ester) + H_2O} \quad \text{(R5)}$$

These accretion reactions involve closed-shell organic compounds, in which all electrons are paired in their molecular orbitals to create stable and less reactive molecules. Therefore, such reactions, hereafter called closed-shell accretion reactions, have high energy barriers. Accretion reactions of the R1−R5 type are therefore unlikely to occur in the gas phase, and most studies on their atmospheric relevance have accordingly focused on studying the condensed phase (e.g., cloud droplets).[25] In addition to closed-shell accretion reactions, also reactions involving radical species as well as high-energy Criegee intermediates (carbonyl oxides) have been suggested to contribute to atmospheric SOA formation.[24] For instance, the reactions of stabilized Criegee intermediates ($\mathrm{RC(CH_3)(OO)}$) with alcohol, water, carboxylic acid, etc. forming adducts of the general type

$$\mathrm{(RC(CH_3)(OR)(OOH))} \quad \text{(R6)}$$

have attracted attention of experimentalists[24] and theoretical studies, such as ref 26, have recently addressed $\mathrm{RO_2 + RO_2 \rightarrow ROOR + O_2}$ reactions. Accretion reactions may also occur in the gas phase. However, the detailed mechanisms are likely to be complex and involve, for example, intersystem crossing. In this study, we focus on the catalysis of closed-shell accretion reactions by small inorganic aerosol models. Catalysis of accretion reactions by single molecules or small molecular clusters can be considered as an intermediate case between gas-phase and condensed-phase chemistry and has recently received increasing attention in atmospheric chemistry.[27−30] However, the central question of "which species are able to catalyze closed-shell accretion reactions?" has not yet been answered conclusively.

To find the species that can catalyze accretion reactions of closed-shell species, we have previously evaluated the effect of ammonia, water, formic acid, and sulfuric acid clusters on six model reactions.[31] The results showed an increase in the rate of the reactions but clarified that the studied clusters cannot catalyze the reactions sufficiently for the process to be competitive in the troposphere. Since mineral dust is abundant in atmospheric aerosols, and closed-shell accretion reactions are unlikely to occur in the gas phase,[24] we now investigate the intrinsic potential of mineral dust for catalyzing nonradical accretion reactions. It should be noted that several experiments have been dedicated to unraveling the role of dust in oxidative formation of SOAs, e.g., refs 32, 33. However, these studies have mainly analyzed and discussed the catalytic role of aged and unprocessed dust particles or surrogate minerals in dissociating ozone molecules and reducing oxidative SOA formation. Therefore, this study complements the information available on the effect of mineral dust on SOA formation. Due to the diversity of the organic compounds that can participate in SOA formation, this study narrows down the list of possible accretion reactions and focuses on the following model reactions

$$\mathrm{CH_2O(formaldehyde) + syn-HCO_2H(formic\ acid) \rightleftharpoons HCO_2CH_2OH} \quad \text{(R7)}$$

$$\mathrm{CH_2O + H_2O \rightleftharpoons CH_2(OH)_2(methanediol)} \quad \text{(R8)}$$

$$\mathrm{CH_3OH(methanol) + syn-HCO_2H \rightleftharpoons CH_3OCHO(methyl\ formate) + H_2O} \quad \text{(R9)}$$

The organic compounds participating in R7−R9 represent the most common organic functional groups in atmospheric chemistry. Furthermore, reactions R7−R9 are relevant for tropospheric accretion product formation since carbonyls,[14] alcohols, and acids[34−36] have all been identified as important precursors for SOAs.[5] To determine the impact of dust aerosols on reactions R7−R9, a chemical kinetics approach is followed. We first explore the reaction mechanisms in the absence and presence of dust aerosols. Next, the impact of mineral dust is quantified by calculating the rate constants of the reactions in the gas phase, and on the surface of dust, using transition-state (TS) theory under representative tropospheric conditions.

2. METHODS

2.1. Computational Details. Gaussian 16 revision A.03[37] was employed to perform all density functional theory (DFT)-based calculations. The geometry optimizations and harmonic frequency calculations were executed using the ωB97X-D density functional[38] with the 6-31++G** basis set. The ωB97X-D functional was specifically used due to the importance of electrostatic long-range exchange−correlation and relative significance of electrostatic correction[39] for the study of the reactions between closed-shell compounds. Moreover, the ωB97X-D functional has been shown to describe noncovalent interactions precisely and give accurate thermochemical and chemical kinetics results.[38,40]

DOI: 10.1021/acs.jpca.9b06331
J. Phys. Chem. A 2019, 123, 9008−9018

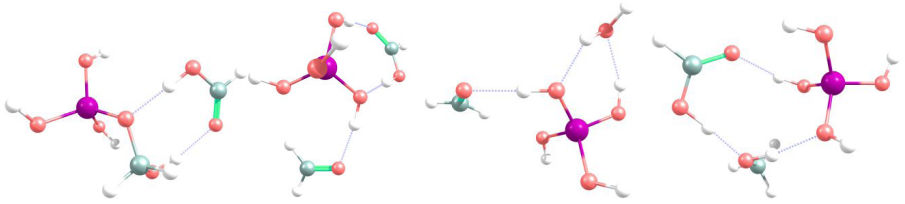

Figure 1. GM structures of the reactants/dust model clusters. The purple, red, gray, and white balls represent silica, oxygen, carbon, and hydrogen, respectively.

Furthermore, ab initio single-point energy calculations were applied to the optimized geometries to increase the accuracy of the final energy profiles. For this purpose, the domain-based local pair-natural orbital (DLPNO)-CCSD(T) method[41−43] was chosen since it has been shown to be an efficient, cost-effective, and accurate method for analyzing thermochemistry of closed-shell organic molecules,[44] providing results close to those of canonical coupled-cluster calculations.[45] Along with the DLPNO-CCSD(T) method, the aug-cc-pVTZ[46,47] basis set, the cc-pVTZ/C auxiliary basis and the tight pair-natural orbital (TightPNO) criterion were used. Using the standard notation of quantum chemistry, the reaction profiles were thus described at the DLPNO-CCSD(T)/aug-cc-pVTZ//ωB97X-D/6-31++G** level of theory. Since the DLPNO-CCSD(T) method is not implemented in Gaussian, Orca 4.1.1[48] was used for the corresponding energy calculations. Calculating single-point coupled-cluster electronic energies for DFT-optimized geometries is a standard approach in computational chemistry, both in atmospheric applications and elsewhere.[49,50]

Benchmarking of the selected level of theory was addressed in our previous study[31] by comparing the Gibbs free energy and activation energies of seven accretion reactions with the values obtained from the high ab initio level of CCSD(T)-F12/VTZ-F12//MP2/aug-cc-pVTZ. The comparison yielded the mean absolute error of 2.3 kJ mol^{-1} for DLPNO-CCSD(T)/aug-cc-pVTZ//ωB97X-D/6-31++G**. The suitability of the computational level was further confirmed by comparing the geometries optimized at the ωB97X-D/6-31++G** level with the available experimental geometries of the reactants and products and, also, the geometries obtained from several computational levels (see Figure S1). Furthermore, the enthalpy of the reactions at 0 K was compared with the available experimental data in Table S1. Both Figure S1 and Table S1 demonstrated appropriateness of the selected level for study of reactions R7−R9.

After validating the computational approach, the reaction mechanisms were explored at the ωB97X-D/6-31++G** level. The stationary structures with nonimaginary frequencies were assigned as reaction intermediates/wells, while the structures with an imaginary frequency were tentatively assigned as transition states (TS). To verify the identity of the TSs, as well as their corresponding reactants and products, intrinsic reaction coordinate[51,52] calculations were performed in both forward and reverse directions. The energy profiles of the resultant reaction paths were obtained by combining the DLPNO-CCSD(T)/aug-cc-pVTZ electronic energies with the ωB97X-D/6-31++G** vibrational zero-point energies (ZPE) for all stationary points.

In the case of the surface-based reactions, the reactants could approach the dust models in many ways. To screen the possible reactant/dust complexes, the artificial bee colony (ABC) algorithm, as embedded in the ABCluster 1.4 program,[53,54] was employed. Using the ABC algorithm, 500 initial reactant/dust configurations were created as the trial population. Each trial structure was adopted as a starting point to generate 500 new structures and search for the local and global minima (GM) structures using 10 scout bees. The energy of each generated complex was considered as the sum of Lennard−Jones and Columbic interactions to give a list of 200 structures as the local minima for each reactant/dust complex. In the next step, the generated local minima were optimized using the GFN-xTB[55] semiempirical method by the XTB 6.0.1 program.[56] After that, the structures were sorted based on their Gibbs free energy values at 298 K and the 30 lowest-energy structures for each reaction were reoptimized at the ωB97X-D/6-31++G** level of theory. The most stable structures from this optimization process were then used to scan the possible reaction paths (see Figure 1 for the global minima (GM) structures of the surface-based reactions related to the smallest dust model). However, in the case of R7 on the smallest model, the GM complex was so stable that forcing the reactants to approach each other ended up with reactant decomposition. Consequently, the corresponding reaction path was deemed to be unfavorable and the less stable complexes were tested to find the representative prereaction complexes and the related TSs.

2.2. Mineral Dust Model Selection and Validation. To evaluate the impact of mineral dust on the studied reactions, an appropriate model dust structure is required. Such a structure is not straightforward to generate as the structure and chemistry of dust aerosols are highly complex and variable. The composition of dust aerosols depends on their sources.[57] Also, their chemical and physical properties change upon aging[58,59] and phase transitions.[58] Moreover, the distribution of mineral components in dust is naturally inhomogeneous[60] and mineral components may have different particle sizes.[60,61] To simplify the problem, we focused on the major dust minerals. Based on numerous studies on dust components, quartz is the major oxide component of mineral dust (40−70%).[62,63] In addition, quartz has been reported as a significant component of different dust samples, e.g., see refs 60, 64−67. Also, feldspars (aluminosilicates) have been shown to contribute considerably to diverse dust samples.[63,67−69] These two classes of minerals form more than 80% of the volume of mineral dust.[70] Besides quartz and feldspars, significant amounts of calcite[63,64,67,69] and clays (such as kaolinite[60,63,69] and illite[68]) have been observed in many dust samples. However, their relative amounts are significantly lower than those of feldspars and quartz.[67] It should be also noted that molten clays can transform into feldspars as they mostly consist of phyllosilicates.[60] Our model dust minerals were thus assumed to contain only feldspars and quartz. Since

DOI: 10.1021/acs.jpca.9b06331
J. Phys. Chem. A 2019, 123, 9008−9018

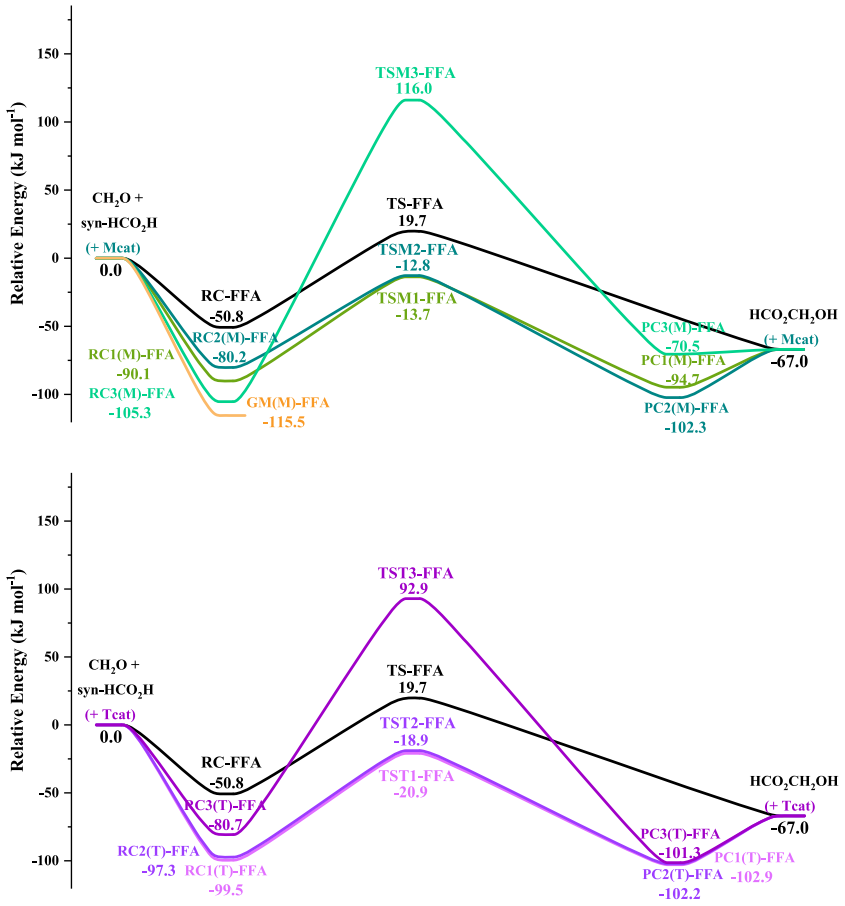

Figure 2. ZPE-corrected potential energy surface of R7 at the DLPNO-CCSD(T)/aug-cc-pVTZ//ωB97X-D/6-31++G** level of theory and 0 K. The black, green and purple reaction paths refer to the gas-phase, Mcat-based and Tcat-based reactions, respectively.

these minerals are mainly composed of silica (SiO_2) units, and closed-shell reactions between neutral molecules require the reactants to be in close proximity to each other, a small silica model should be sufficient for representing mineral dust aerosols. Accordingly, monosilicic acid (Mcat, $Si(OH)_4$) was chosen as the basic model of mineral dust. To investigate the effect of dust model size on our results, linear trisilicic acid (Tcat, $Si_3O_2(OH)_8$) was also considered, as suggested by Ji et al.[62] Although silicic acid has been accepted as the best geometrical and chemical model of SiO_2 minerals,[62,71−73] the model choices were further validated by comparing their optimized geometries with several quartz, feldspar, and clay crystal structures (see Table S2). Based on the geometrical parameters outlined in this table, both Mcat and Tcat can capture the general geometrical features of silica-based minerals. Therefore, they were chosen to represent dust aerosols.

3. RESULTS AND DISCUSSION

3.1. Reaction Mechanism. To understand the effect of mineral dust on closed-shell accretion reactions, the mechanism of reactions R7−R9 was first explored in the gas phase. Figures 2−4 show the potential energy surfaces (PESs), and Figures S2−S4 present the geometries of the corresponding stationary points. It should be noted that, in these figures, the stationary points (reactant complexes and transition states) involved in reaction R7 (the reaction between formaldehyde and formic acid; F and FA) are distinguished by including the acronym "FFA" in their names, while the names of the stationary points involved in reaction R8 (the reaction between formaldehyde and water; F and W) contain "FW", and those of reaction R9 (the reaction between formic acid and methanol; FA and M) contain "FAM". Also, numerical identities have been attributed to all stationary points to distinguish between the species related to each reaction.

As can be seen in Figures 1−3, the entrance channels of all three reactions are barrierless. This means that when the reactants are at large separations, they should be able to overcome the centrifugal barrier to approach each other, and form a prereaction complex, at rates comparable to the gas-kinetic collision rate. The generated prereaction complexes can then pass over TS-FFA (19.7 kJ mol^{-1}) and TS-FW (152.4 kJ mol^{-1}) (see Figure 5 for their structures) to give the final products of reactions R7 and R8, respectively. In the case of R9, the reaction can follow two different paths to produce the accretion products. Along the first path, the prereaction complex undergoes intermolecular hydrogen transfer from the −OH group of methanol to the carbonyl oxygen (O═C) of formic acid, simultaneous with the formation of a C−O bond between the two reactants (TS1-FAM; 132.6 kJ mol^{-1}), producing the INT intermediate (−14.8 kJ mol^{-1}) (see Figures 5 and S4 for the geometries). Next, internal hydrogen transfer from one hydroxyl group of INT to another, together with gradual cleavage of the O−H bond of the hydrogen receptor hydroxyl group (TS2-FAM; 142.5 kJ mol^{-1}), yields water and CH_3OCHO. Along the second path, the hydrogen from the hydroxyl group of methanol is directly transferred to the

DOI: 10.1021/acs.jpca.9b06331
J. Phys. Chem. A 2019, 123, 9008−9018

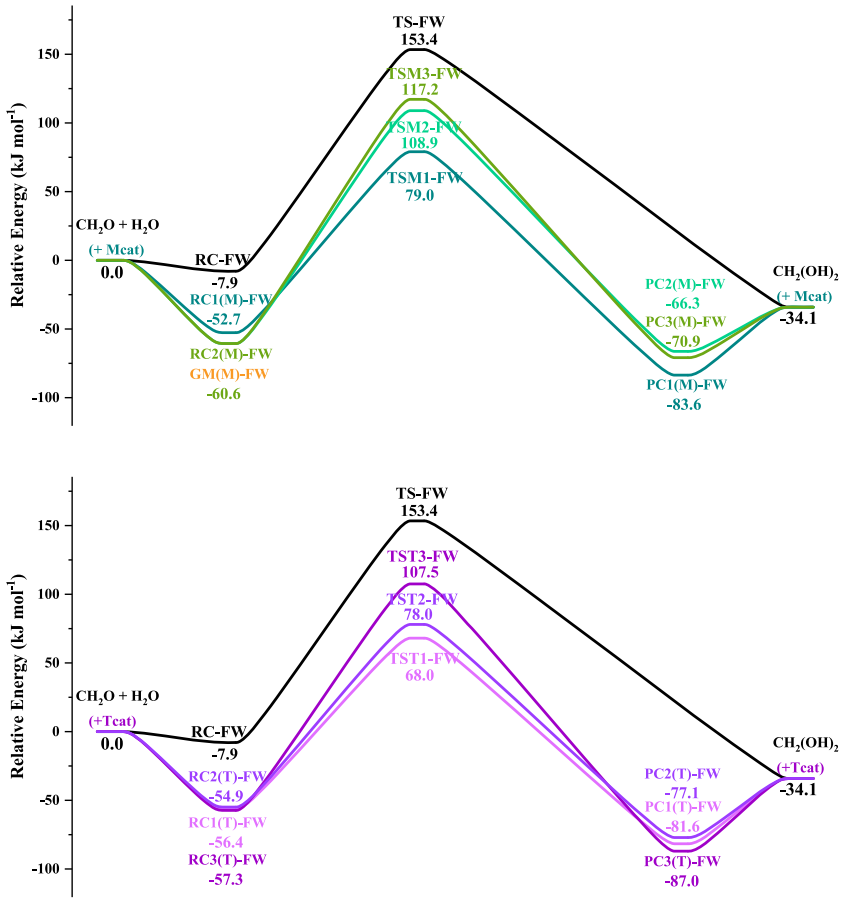

Figure 3. ZPE-corrected potential energy surface of R8 at the DLPNO-CCSD(T)/aug-cc-pVTZ//ωB97X-D/6-31++G** level of theory and 0 K. The black, green, and purple reaction paths refer to the gas-phase, Mcat-based, and Tcat-based reactions, respectively.

hydroxyl group of formic acid, simultaneous with the formation of a C−O bond between the two reactants and cleavage of the O−H bond in formic acid (TS3-FAM; 158.9 kJ mol^{-1}). This results in a weakly bound postreaction complex that later dissociates into the individual water and CH_3OCHO products.

Regardless of their detailed mechanisms and energy profiles, the gas-phase reactions R7−R9 share two general features: they all involve relatively stable prereaction complexes and their rates are limited by high reaction barriers. The apparent barrier heights, i.e., the barrier energies relative to the free reactants, range from 19.6 (TS-FFA; R7) to 158.9 (TS3-FAM; R9) kJ mol^{-1} at 0 K. A close look at the structures of the TSs (see Figure 5) suggests that the strain caused by formation of ringlike geometries destabilizes the TSs,[31] while hydrogen bonding stabilizes them. This hypothesis is supported by comparing the geometry of TS-FFA with a six-membered ring and the lowest barrier height (19.6 kJ mol^{-1}) to the geometry of the other TSs with four-membered rings and barrier heights above 130 kJ mol^{-1}.

The fundamental question of this study concerns the effect of mineral dust on the reactions. Therefore, the reaction mechanisms were also investigated in the presence of the mineral dust models. To facilitate distinguishing the stationary points of the dust-assisted and gas-phase reactions, (M) or M is added to the notation of the Mcat-based reactions. Similarly, (T) and T in the notation refer to the Tcat-based reactions. When Mcat is added to the reactive system, the reactants can form hydrogen bonds with the hydroxyl groups of Mcat. See Figures S2−S4 for illustrations of all prereaction geometries, and Figure 6 for the prereaction complexes of reaction R7, which are very close in energy but involve different orientations of the reaction products. The additional hydrogen bonds stabilize the reactant complexes to a much greater extent compared to the gas-phase reaction (see Figures 2−4).

After forming the prereaction complexes, two factors determine the fate of the adsorbed reactants: the extent of stabilization and the relative orientation of the reactants. Figures 2 and 6 illustrate this, and show that the well-oriented reactants in the prereaction complexes RC1(M)-FFA and RC2(M)-FFA (Mcat-based R7) can easily convert into products by passing over the submerged barriers corresponding to transition states TSM1-FFA and TSM2-FFA, which are respectively 13.7 and 12.8 kJ mol^{-1} below the energy level of the free reactants at 0 K. However, in the RC3(M)-FFA complex, the two reactants are stabilized by different hydroxyl groups. This inappropriate orientation causes their large separation, leads to a very high energy barrier (TSM3-FFA; 116.0 kJ mol^{-1} above the free reactants). It should be noted that TSM3 is 96.3 kJ mol^{-1} higher than the gas-phase barrier (TS-FFA), while TSM1 and TSM2 are 33.4 and 32.5 kJ mol^{-1} lower than the gas-phase barrier, respectively. In the case of R8 and R9, Mcat reduces the barrier of all reaction paths by about 18.5−74.4 kJ mol^{-1}.

According to the outlined energy profiles, the performance of dust minerals in surface-based accretion reactions strongly depends on the starting configurations of the reactant/Mcat clusters. The different orientations of the reactants toward the

DOI: 10.1021/acs.jpca.9b06331
J. Phys. Chem. A 2019, 123, 9008−9018

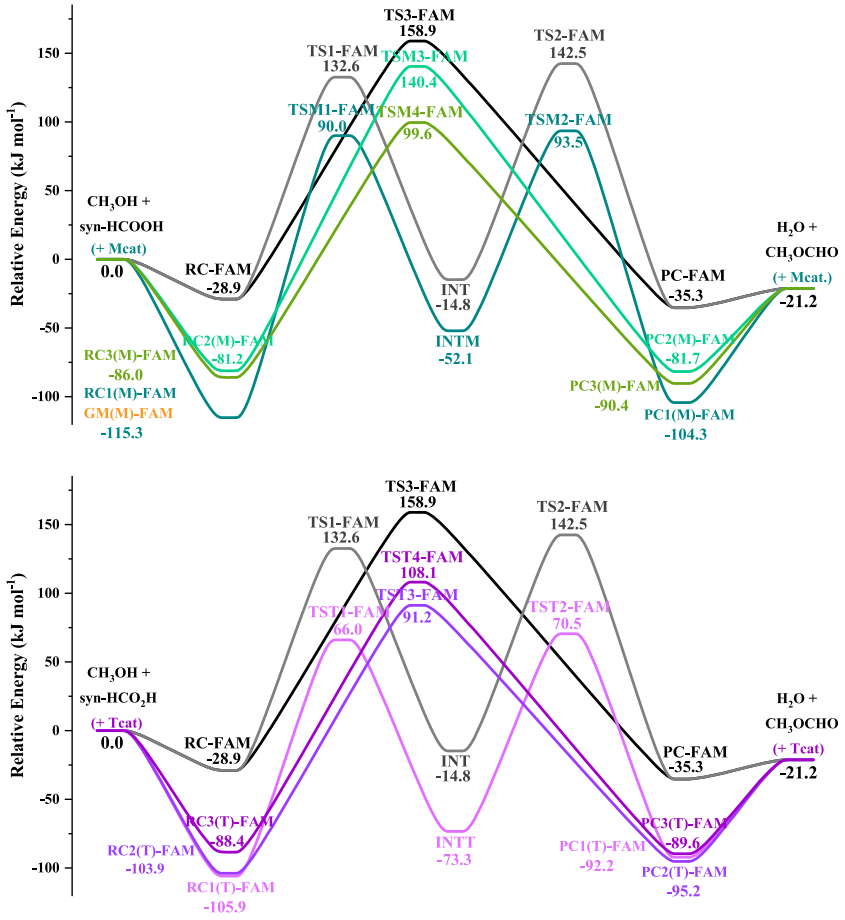

Figure 4. ZPE-corrected potential energy surface of R9 at the DLPNO-CCSD(T)/aug-cc-pVTZ//ωB97X-D/6-31++G** level of theory and 0 K. The black (and gray), green, and purple reaction paths refer to the gas-phase, Mcat-based, and Tcat-based reactions, respectively.

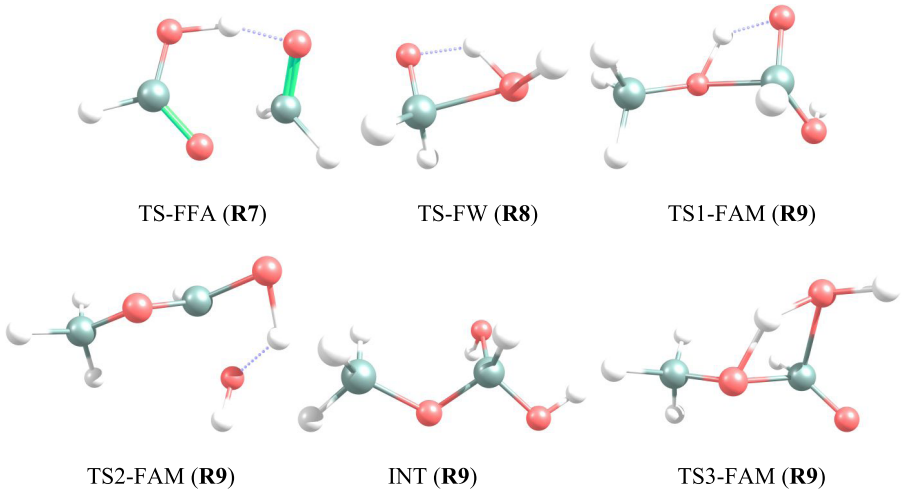

Figure 5. Transition-state geometries of gas-phase R7−R9 reactions. The blue dotted lines represent hydrogen bonding. The red, gray and white balls represent oxygen, carbon and hydrogen, respectively.

surface and each other create multiple reaction paths with highly variable barriers. Along some reaction paths, mineral dust may inhibit the reaction due to the inappropriate relative orientation of the reactants in the reactant complexes. On the other hand, along some reaction paths, the favorable orientation of reactants on mineral dust assists the conversion of reactants into the products. The combination (and competition) of these two determines whether or not mineral dust acts as a catalyst for a particular reaction. In any case, the surface hydroxyl groups of dust minerals are predicted to have a noticeable role in stabilization of the reactants. They also stabilize the reaction products by forming postreaction complexes and also increase the stability of the INT intermediate for R9. It should be noted that in the gas-phase our calculations predict the existence of a postreaction complex for only R9.

DOI: 10.1021/acs.jpca.9b06331
J. Phys. Chem. A 2019, 123, 9008−9018

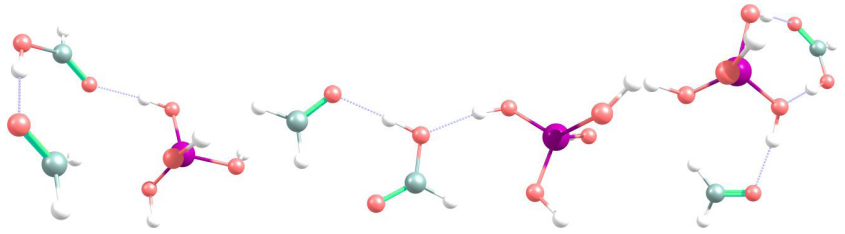

Figure 6. Prereaction complexes of Mcat-based reaction of formaldehyde with formic acid (R7). The blue dotted lines represent hydrogen bonding. The silica, oxygen, carbon, and hydrogen atoms are shown as purple, red, gray, and white balls, respectively.

The reaction mechanisms were also evaluated in the presence of Tcat to analyze the effect of a larger dust unit with more accessible silica atoms and hydroxyl groups. As illustrated in Figures 2−4, access to more adsorption sites, i.e., more hydroxyl groups, affects the energies of the various pre- and postreaction complexes in different ways. Some pre- and postreaction complexes are less stable than their Mcat-based counterparts, while the others are more stable. Another general feature of the Tcat-based reactions is that many of the related pre- and postreaction complexes have similar relative energies, e.g., RC1(T)-FFA and RC2(T)-FFA (R7), PC1(T)-FFA and PC2(T)-FFA (R7), RC1(T)-FW, RC2(T)-FW and RC3(T)-FW (R8), and RC1(T)-FAM and RC2(T)-FAM (R9). However, they have distinguishable structures as shown in Figures 6 and S2−S4. Despite variations in the relative energies and configurations of the prereaction complexes, the use of Tcat lowers the overall barrier heights in all cases. Also, INT (−14.8 kJ mol^{-1}; R9) can be noticeably stabilized by Tcat (INTT: −73.3 kJ mol^{-1}) compared to Mcat (INTM: −52.1 kJ mol^{-1}). In general, Tcat acts more effective than Mcat in reducing the barrier heights, which means that larger mineral dust catalytic sites are more effective than the smaller sites in assisting the progress of the studied accretion reactions.

3.2. Catalytic Efficiency in the Troposphere. The detailed PESs reported in Figures 2−4 are not sufficient for determining the catalytic role of mineral dust in atmospheric conditions since the presented energy profiles ignore thermal and entropic contributions. Also, the overall atmospheric importance of the catalytic reactions depends on the concentration of catalytic sites. To quantitatively estimate the effect of mineral dust on the extent of the studied accretion reactions, the rates of the surface-based and gas-phase reactions under tropospheric conditions should be calculated. The rate expressions of the reactions were written in the general form of eq 1, where k is the total rate constant of the reaction, squared brackets denote concentrations, and the number of "reactants" m equals 2 for gas-phase reactions and 3 for the surface-based reactions (where the catalyst is included as a "reactant" for the purpose of evaluating the rate).

$$\text{rate} = k \times \prod_{i=1}^{m} [(\text{reactant})_i] \tag{1}$$

To determine whether mineral dust can really catalyze the studied accretion reactions, we define the catalytic enhancement (CE) parameter as the ratio of the catalyzed reaction rate to the gas-phase rate.[74] In adopting this definition, we implicitly assume that the kinetics of the surface-based reactions is controlled by the chemical reaction rather than the diffusion process of reactants to the surface. This means that we assume that the same concentrations of water, formaldehyde, formic acid, and methanol reactants are available for both gas-phase and surface-based reactions. Under this assumption, the enhancement of the accretion reactions depends only on the concentration of Mcat or Tcat and the k values of the gas-phase and surface-based reactions. To calculate the rate coefficients of the reactions, tunneling-corrected transition-state theory was applied to the PESs, yielding the following expression

$$k = \kappa_r \times \frac{k_\beta T}{h} e^{-\Delta_r^{\#} G/RT} \tag{2}$$

In this equation, κ_r is the tunneling coefficient, k_B is the Boltzmann constant, h is the Plank constant, T is the temperature, R is the universal gas constant, and $\Delta_r^{\#} G$ is the difference between the Gibbs free energy of the corresponding TS (G_{TS}) and the free reactants ($G_{reactants}$); see eq 3 for details. Note that for the surface-based reactions the free "reactants" include Mcat or Tcat. The tunneling effect is specifically emphasized in eq 2 since the tropospheric reactions take place at temperatures below 300 K, where tunneling may be important especially for reactions involving the motion of hydrogens or protons. To calculate κ_r, the reaction barriers were described as unsymmetrical Eckart barriers.[75] Our kinetic treatment implicitly assumes that the reactants are in equilibrium with the prereaction complexes and that the different prereaction complexes can interconvert into each other (see Table S3 for the Gibbs free energies of the pre- and postreaction complexes). Under such conditions, the exact energies of the prereaction complexes do not affect the rate constants of the reactions.[74] Note that neglecting the prereaction complexes or using the steady-state approximation and including the conversion of the prereaction complexes to the postreaction complexes, as done in ref 76, give the same final rate constant equation. Also, in the case of the two-step reaction path of R9, the rate-determining step was assumed to be the TS with the highest absolute G_{TS}. To be more specific, TS2-FAM, TSM2-FAM, and TST2-FAM were identified as the rate-determining barriers on the two-step paths of the gas-phase, Mcat-, and Tcat-based R9 reactions, respectively. To obtain the G values of the species at the DLPNO-CCSD(T)/aug-cc-pVTZ//ωB97X-D/6-31++G** (DLPNO-DFT) level of theory, the electronic energy obtained from single-point energy calculation at the DLPNO-CCSD(T)/aug-cc-pVTZ level (E_{DLPNO}) was summed with the thermal contribution to Gibbs free energy retrieved from the ωB97X-D/6-31++G** frequency calculations ($G_{thermal}^{DFT}$) (eq 4)

$$\Delta_R^{\#} G = G_{TS} - G_{reactants} \tag{3}$$

DOI: 10.1021/acs.jpca.9b06331
J. Phys. Chem. A 2019, 123, 9008−9018

Table 1. CE/[Mcat or Tcat] and Estimated CE Values of R7, R8, and R9 in the Presence of Mcat and Tcat at Atmospherically Representative Concentrations of Catalyst Sites per Unit Volume

	CE/[Mcat or Tcat]		CE	
	298.15 K	198.15 K	298.15 K	198.15 K
R7 (Mcat)	2.35×10^{-2}	1.92×10^{1}	3.61×10^{-20}–3.61×10^{-19}	1.95×10^{-17}–1.95×10^{-16}
R7 (Tcat)	3.33×10^{-1}	8.87×10^{2}	2.38×10^{-19}–3.61×10^{-18}	4.20×10^{-16}–4.20×10^{-15}
R8 (Mcat)	1.05×10^{4}	7.18×10^{10}	1.61×10^{-14}–1.61×10^{-13}	7.31×10^{-8}–7.31×10^{-7}
R8 (Tcat)	9.64×10^{5}	4.35×10^{13}	6.87×10^{-13}–6.87×10^{-12}	2.06×10^{-5}–2.06×10^{-4}
R9 (Mcat)	5.36×10^{-1}	1.41×10^{4}	8.21×10^{-19}–8.21×10^{-18}	1.43×10^{-14}–1.43×10^{-13}
R9 (Tcat)	7.17×10^{2}	1.98×10^{9}	5.11×10^{-16}–5.11×10^{-15}	9.40×10^{-10}–9.40×10^{-9}

$$G_{\mathrm{DLPNO-DFT}} = E_{\mathrm{DLPNO}} + G^{\mathrm{DFT}}_{\mathrm{thermal}} \quad (4)$$

Finally, implementing eq 2 for all possible reaction paths in our definition of CE resulted in the following general equation

$$\mathrm{CE} = \frac{[\mathrm{catalyst}]}{\kappa_{\mathrm{r0}}} \sum_{i=1}^{n} \kappa_{\mathrm{ri}} \times \mathrm{e}^{(\Delta^{\#}_{\mathrm{r0}}G - \Delta^{\#}_{\mathrm{ri}}G)/RT} \quad (5)$$

Here, the subscripts "ri" and "r0" denote the surface-based and gas-phase reactions, respectively, for all n reaction paths, and CE can be considered dimensionless by expressing catalyst concentration as the ratio of catalyst pressure in the atmosphere to the reference pressure used in the $\Delta^{\#}_{\mathrm{r}}G$ calculations (1 atm), which makes the ratio CE/[catalyst] a dimensionless number. Table S4 reports the $\Delta^{\#}_{\mathrm{r}}G$ and κ_{r} values of the R7, R8, and R9 reaction paths computed at 198 and 298 K (1 atm) and embedded in eq 5. Based on Table S4, the tunneling effect is more profound in the case of the gas-phase reactions and at the lower temperature of 198 K, as expected. In addition, tunneling varies significantly from one reaction path to another due to the differences in the barrier heights and the associated imaginary frequencies. The combined effect of the variations in barrier height, imaginary frequency, and temperature leads to κ_{r} values ranging from 1.88 to 8.02.

A fact highlighted by Table S4 is that the energy profiles of the studied reactions are quite sensitive to the thermal contributions. For example, for the surface-based R7 reaction paths, the TSs are below the reactants according to their ZPE-corrected energies but above the reactants in terms of free energy at 298 K. On the other hand, the thermal contribution is not sufficient at 198 K to raise the TSs above the reactants. The thermal contribution at 198 K is naturally lower than that of 298 K also for R8 and R9. Interestingly, along some reaction paths of R8 and R9, consideration of thermal contribution gives surface-based reaction barriers that are lower than the barrier of the gas-phase reactions, see for example the "r1 (TSM1-FW)" reaction path of R8 at 298 K in Table S4. Table S4 also shows that mineral dust catalysis reduces the enthalpy barriers of the reactions ($\Delta^{\#}_{\mathrm{r}}H$) along most reaction paths, which is not surprising as enthalpy and ZPE-corrected electronic energy are similar to each other. However, as adsorption of the reactants on the surface of mineral dust limits their translational freedom, the entropy of the reactions ($\Delta^{\#}_{\mathrm{r}}S$) decreases on the surface of Mcat and Tcat and the reactions become entropically less favorable. In the case of R7 and R9 (both at 298 K), the decrease of enthalpy does not compensate for the negative effect of entropy reduction, while the decrease of enthalpy can compensate for the impact of entropy reduction for R7 (198 K), R8 (198 and 298 K), and R9 (198 K).

Since CE depends on the $\Delta^{\#}_{\mathrm{r}}G$ and κ_{r} values (see eq 5), the discussed thermochemical changes are reflected in the CE/[catalyst] results, which are outlined in Table 1. If we ignore the effect of catalyst concentration and just focus on the CE/[catalyst] values, mineral dust seems to be able to catalyze all three reactions at 198 K. However, the CE/[catalyst] values clearly show that both Mcat and Tcat inhibit R7 at 298 K by elevating the reaction barrier. The CE/[catalyst] results also show that Tcat outperforms Mcat in lowering the barrier height for all reactions and, therefore, increasing the rate of all studied reactions. Therefore, if we just rely on the CE/[catalyst] results, mineral dust would seem to be able to catalyze all reactions at 198 K and thus enhance SOA formation. In particular, the CE/[catalyst] values suggest that each Tcat site can catalyze the R8 reaction up to factors of 9.64×10^{5} and 4.35×10^{13} at 298 and 198 K, respectively. The CE/[catalyst] values of R7 and R9 are also higher at 198 K. In other words, based on the CE/[catalyst] results, mineral dust seems to enhance the accretion reactions more significantly at higher altitudes in the troposphere, where the temperature is lower. Furthermore, CE/[catalyst] results would indicate that, at lower altitudes (298 K), dust aerosols would act more selectively by retarding R7 while enhancing R8 and R9. It should be added that neither the CE nor the CE/[catalyst] values depend significantly on the number of the reaction paths offered by the dust surface, as some reaction paths are far less feasible than the others, CE is dominated by the most favorable path (highest rate coefficient k).

Finally, we estimated the catalyst concentrations ([Mcat] and [Tcat]) to determine whether catalysis of accretion reactions by mineral dust is an important process in the real atmosphere. For this purpose, we defined [Mcat] and [Tcat] as the number concentration of the catalytic sites (number of Mcat or Tcat sites per volume of air). To find an appropriate range of values, the typical surface area concentration of dust aerosol was taken to be 1.0×10^{-6}–1.0×10^{-7} $\mathrm{cm^2\ cm^{-3}}$, according to the values reported in refs 77–80. Then, the total number of active sites present in the tropospheric dust aerosols per unit volume of air (i.e., [catalyst]) was obtained by dividing this total surface area concentration of mineral dust aerosols by the surface area of Mcat (25.76 $\mathrm{Å^2}$) or Tcat (55.33 $\mathrm{Å^2}$) (calculated using ChemCraft 1.8[81]). The resultant catalyst concentrations (in $\mathrm{cm^{-3}}$, which should be interpreted as the number of catalytic sites per $\mathrm{cm^3}$ of air) were then converted into the unit of atm by applying the ideal gas law. As presented in Table 1, the CE values are below 10^{-3} for all reactions and reaction conditions, which shows that mineral dust aerosols cannot contribute significantly to the progress of atmospheric accretion reactions of closed-shell compounds. It should be added that the relatively low concentration of catalytic sites in the troposphere is not the only reason behind the negligible

DOI: 10.1021/acs.jpca.9b06331
J. Phys. Chem. A 2019, 123, 9008–9018

CE values. Another important reason is that the bimolecular k values of many of the studied gas-phase and surface-based reaction paths are lower than 10^{-37} cm^3 molecule^{-1} s^{-1}, under tropospheric conditions, with only a few of the R7 reaction paths reaching k values above 10^{-20} cm^3 molecule^{-1} s^{-1}. Thus, even if the relative enhancement of the rates due to the presence of mineral dust is in some cases enormous, the absolute reaction rates are still extremely slow in an atmospheric chemistry context.

4. CONCLUSIONS

To find the atmospheric species or particles that might catalyze formation of secondary organic aerosols in the troposphere, we investigated the role of mineral dust in dimerization kinetics of model closed-shell organic compounds (R7−R9). By analyzing the reaction mechanism at 0 K, mineral dust was found to have the potential for enhancing adsorption of the reactants, directing them toward prereaction complex formation, reducing the barrier heights and stabilizing the postreaction complexes. This would strongly increase the formation rate of dimers that are less volatile than the original organic compounds. However, inclusion of thermal effects (using a temperature range of 198−298 K relevant to the troposphere) leads to a significant decrease in the predicted catalytic effect due to the entropy penalty associated with clustering of the reactants with the catalytic sites. The magnitude of this penalty increases with temperature and thus opposite to altitude in the troposphere.

If the effect of catalyst (dust aerosol) concentration be neglected, dust aerosols would enhance the reaction of water and formaldehyde in the lower part of the troposphere (with temperatures close to 298 K). In contrast, dust particles tend to inhibit the reaction of formaldehyde with formic acid. The reaction of methanol with formic acid at 298 K is only enhanced if a sufficient number of silica bound hydroxyl groups be available for stabilizing the reacting species. In the upper troposphere (with temperatures closer to 198 K), mineral dust is able to enhance all three studied reactions. In particular, mineral dust would have a drastic impact on the reaction of water with formaldehyde toward $CH_2(OH)_2$ production if a sufficient amount of mineral dust aerosols be available. In other words, R8 would have the greatest contribution to SOA formation in the presence of abundant mineral dust catalytic sites.

Furthermore, the inherent catalytic effect of reactions R7 (formaldehyde reaction with formic acid), R8 (formaldehyde reaction with water), and R9 (formic acid reaction with methanol) were also calculated for molecular clusters of water (R7, 4.05×10^{-2} and R8, 1.37×10^{8}) and sulfuric acid (R7, 2.39×10^{6}; R8, 7.08×10^{24}; and R9, 7.43×10^{22}) at 298 K, without including tunneling effects, based on the data of ref 31. The calculations revealed that when catalyst concentrations are neglected, sulfuric acid outperforms both mineral dust (Tcat: R7, 3.13×10^{-1}; R8, 9.64×10^{5}; and R9, 7.17×10^{2}) and water in increasing SOA formation through the accretion reaction of the studied closed-shell organic compounds.

Finally, the reactions were analyzed in a more realistic context by including the likely concentration range of active mineral dust sites in the atmosphere, allowing an estimation of the absolute values for the catalytic effect (CE). This analysis revealed that dust aerosols are not capable of contributing to atmospheric SOA formation through accretion reactions. The reasons for this are the insufficient concentration of active sites, and the relatively low absolute rate constants of the surface-based reactions. In contrast, sulfuric acid at atmospheric concentrations of around 1×10^{6} molecule cm^{-3}[82] is indeed able to enhance some closed-shell accretion reactions (CE: R7, 9.43×10^{-14}; R8, 2.79×10^{5}; and R9, 2.93×10^{3}).

■ ASSOCIATED CONTENT

Supporting Information

The Supporting Information is available free of charge on the ACS Publications website at DOI: 10.1021/acs.jpca.9b06331.

Cartesian coordinates and the geometries of the silica models, reactants, products, transition states, and reaction complexes; reaction enthalpies at different levels of theory; imaginary frequencies of the transition states; tunneling coefficients; reaction Gibbs free energies (PDF)

Output files for single-point energy and frequency calculation on all structures (ZIP)

■ AUTHOR INFORMATION

Corresponding Author

*E-mail: fatemeh.keshavarz@helsinki.fi.

ORCID

Fatemeh Keshavarz: 0000-0003-2189-7809

Hanna Vehkamäki: 0000-0002-5018-1255

Theo Kurtén: 0000-0002-6416-4931

Notes

The authors declare no competing financial interest.

■ ACKNOWLEDGMENTS

We thank the Academy of Finland University of Helsinki, Faculty of Science ATMATH Project, and the ERC Project 692891-DAMOCLES for funding and the CSC-IT Center for Science in Espoo, Finland, for computational resources.

■ REFERENCES

(1) Carlton, A. G.; Wiedinmyer, C.; Kroll, J. H. A Review of Secondary Organic Aerosol (SOA) Formation from Isoprene. *Atmos. Chem. Phys.* **2009**, *9*, 4987−5005.

(2) Novakov, T.; Penner, J. E. Large Contribution of Organic Aerosols to Cloud-Condensation-Nuclei Concentrations. *Nature* **1993**, *365*, 823−826.

(3) Andreae, M. O.; Crutzen, P. J. Atmospheric Aerosols: Biogeochemical Sources and Role in Atmospheric Chemistry. *Science* **1997**, *276*, 1052−1058.

(4) Pope, C. A., III; Ezzati, M.; Dockery, D. W. Fine-Particulate Air Pollution and Life Expectancy in the United States. *N. Engl. J. Med.* **2009**, *360*, 376−386.

(5) Kalberer, M.; Paulsen, D.; Sax, M.; Steinbacher, M.; Dommen, J.; Prevot, A. S. H.; Fisseha, R.; Weingartner, E.; Frankevich, V.; Zenobi, R.; Baltensperger, U. Identification of Polymers as Major Components of Atmospheric Organic Aerosols. *Science* **2004**, *303*, 1659−1662.

(6) Geddes, S.; Zahardis, J.; Petrucci, G. A. Chemical Transformations of Peptide Containing Fine Particles: Oxidative Processing, Accretion Reactions and Implications to the Atmospheric Fate of Cell-Derived Materials in Organic Aerosol. *J. Atmos. Chem.* **2009**, *63*, 187−202.

(7) Kanakidou, M.; Seinfeld, J. H.; Pandis, S. N.; Barnes, I.; Dentener, F. J.; Facchini, M. C.; Dingenen, R. V.; Ervens, B.; Nenes, A. N. C. J. S. E.; Nielsen, C. J.; Swietlicki, E. Organic Aerosol and Global Climate Modelling: A Review. *Atmos. Chem. Phys.* **2005**, *5*, 053−1123.

DOI: 10.1021/acs.jpca.9b06331
J. Phys. Chem. A 2019, 123, 9008−9018

(8) Tu, P.; Johnston, M. V. Particle Size Dependence of Biogenic Secondary Organic Aerosol Molecular Composition. *Atmos. Chem. Phys.* **2017**, *17*, 7593−7603.
(9) Seinfeld, J. H.; Pandis, S. N. *Atmospheric Chemistry and Physics: From Air Pollution to Climate Change*; John Wiley & Sons, 2016.
(10) Odum, J. R.; Hoffmann, T.; Bowman, F.; Collins, D.; Flagan, R. C.; Seinfeld, J. H. Gas/Particle Partitioning and Secondary Organic Aerosol Yields. *Environ. Sci. Technol.* **1996**, *30*, 2580−2585.
(11) Robinson, A. L.; Donahue, N. M.; Shrivastava, M. K.; Weitkamp, E. A.; Sage, A. M.; Grieshop, A. P.; Lane, T. E.; Pierce, J. R.; Pandis, S. N. Rethinking Organic Aerosols: Semivolatile Emissions and Photochemical Aging. *Science* **2007**, *315*, 1259−1262.
(12) Lim, H. -J.; Turpin, B. J. Origins of Primary and Secondary Organic Aerosol in Atlanta: Results of Time-Resolved Measurements during the Atlanta Supersite Experiment. *Environ. Sci. Technol.* **2002**, *36*, 4489−4496.
(13) Zhao, Z.; Xu, Q.; Yang, X.; Zhang, H. Heterogeneous Ozonolysis of Endocyclic Unsaturated Organic Aerosol Proxies: Implications for Criegee Intermediate Dynamics and Later-generation Reactions. *ACS Earth Space Chem.* **2019**, *33*, 344−356.
(14) Li, Y. J.; Lee, A. K. Y.; Lau, A. P. S.; Chan, C. K. Accretion Reactions of Octanal Catalyzed by Sulfuric Acid: Product Identification, Reaction Pathways, and Atmospheric Implications. *Environ. Sci. Technol.* **2008**, *42*, 7138−7145.
(15) Turpin, B. J.; Saxena, P.; Andrews, E. Measuring and Simulating Particulate Organics in the Atmosphere: Problems and Prospects. *Atmos. Environ.* **2000**, *34*, 2983−3013.
(16) Barsanti, K. C.; Pankow, J. F. Thermodynamics of the Formation of Atmospheric Organic Particulate Matter by Accretion Reactions—2. Dialdehydes, Methylglyoxal, and Diketones. *Atmos. Environ.* **2005**, *39*, 6597−6607.
(17) Djikaev, Y. S.; Ruckenstein, E. Effect of Heterogeneous Chemical Reactions on the Köhler Activation of Aqueous Organic Aerosols. *J. Phys. Chem. A* **2018**, *122*, 4322−4337.
(18) Lim, Y. B.; Tan, Y.; Perri, M. J.; Seitzinger, S. P.; Turpin, B. J. Aqueous Chemistry and its Role in Secondary Organic Aerosol (SOA) Formation. *Atmos. Chem. Phys.* **2010**, *10*, 10521−10539.
(19) Rudich, Y.; Donahue, N. M.; Mentel, T. F. Aging of Organic Aerosol: Bridging the Gap between Laboratory and Field Studies. *Annu. Rev. Phys. Chem.* **2007**, *58*, 321−352.
(20) Tobias, H. J.; Ziemann, P. J. Thermal Desorption Mass Spectrometric Analysis of Organic Aerosol Formed from Reactions of 1-Tetradecene and O_3 in the Presence of Alcohols and Carboxylic Acids. *Environ. Sci. Technol.* **2000**, *34*, 2105−2115.
(21) Jang, M.; Kamens, R. M. Atmospheric Secondary Aerosol Formation by Heterogeneous Reactions of Aldehydes in the Presence of a Sulfuric acid Aerosol Catalyst. *Environ. Sci. Technol.* **2001**, *35*, 4758−4766.
(22) Barsanti, K. C.; Pankow, J. F. Thermodynamics of the Formation of Atmospheric Organic Particulate Matter by Accretion Reactions—Part 1: Aldehydes and Ketones. *Atmos. Environ.* **2004**, *38*, 4371−4382.
(23) Johnson, D.; Jenkin, M. E.; Wirtz, K.; Martin-Reviejo, M. Simulating the Formation of Secondary Organic Aerosol from the Photooxidation of Aromatic Hydrocarbons. *Environ. Chem.* **2005**, *2*, 35−48.
(24) Kroll, J. H.; Seinfeld, J. H. Chemistry of Secondary Organic Aerosol: Formation and Evolution of Low-Volatility Organics in the Atmosphere. *Atmos. Environ.* **2008**, *42*, 3593−3624.
(25) Casale, M. T.; Richman, A. R.; Elrod, M. J.; Garland, R. M.; Beaver, M. R.; Tolbert, M. A. Kinetics of Acid-Catalyzed Aldol Condensation Reactions of Aliphatic Aldehydes. *Atmos. Environ.* **2007**, *41*, 6212−6224.
(26) Valiev, R. R.; Hasan, G.; Salo, V. -T.; Kubecka, J.; Kurten, T. Intersystem Crossings Drive Atmospheric Gas-Phase Dimer Formation. *J. Phys. Chem. A* **2019**, *123*, 6596−6604.
(27) Louie, M. K.; Francisco, J. S.; Verdicchio, M.; Klippenstein, S. J.; Sinha, A. Dimethylamine Addition to Formaldehyde Catalyzed by a Single Water Molecule: A Facile Route for Atmospheric Carbinolamine Formation and Potential Promoter of Aerosol Growth. *J. Phys. Chem. A* **2016**, *120*, 1358−1368.
(28) Patil, M. P.; Sunoj, R. B. Insights on Co-Catalyst-Promoted Enamine Formation between Dimethylamine and Propanal through Ab Initio and Density Functional Theory Study. *J. Org. Chem.* **2007**, *72*, 8202−8215.
(29) Sayer, J. M.; Jencks, W. P. Mechanism and Catalysis of 2-methyl-3-thiosemicarbazone Formation. Second Change in Rate determining Step and Evidence for a Stepwise Mechanism for Proton Transfer in a Simple Carbonyl Addition Reaction. *J. Am. Chem. Soc.* **1973**, *95*, 5637−5649.
(30) Duporté, G.; Riva, M.; Parshintsev, J.; Heikkinen, E.; Barreira, L. M.; Myllys, N.; Heikkinen, L.; Hartonen, K. M.; Kulmala, M.; Ehn, M.; et al. Chemical Characterization of Gas- and Particle-Phase Products from the Ozonolysis of α-Pinene in the Presence of Dimethylamine. *Environ. Sci. Technol.* **2017**, *51*, 5602−5610.
(31) Hirvonen, V.; Myllys, N.; Kurtén, T.; Elm, J. Closed-Shell Organic Compounds Might Form Dimers at the Surface of Molecular Clusters. *J. Phys. Chem. A* **2018**, *122*, 1771−1780.
(32) Liu, C.; Chu, B.; Liu, Y.; Ma, Q.; Ma, J.; He, H.; Li, J.; Hao, J. Effect of Mineral Dust on Secondary Organic Aerosol Yield and Aerosol Size in α-pinene/NOx Photo-Oxidation. *Atmos. Environ.* **2013**, *77*, 781−789.
(33) Usher, C. R.; Michel, A. E.; Stec, D.; Grassian, V. H. Laboratory Studies of Ozone Uptake on Processed Mineral Dust. *Atmos. Environ.* **2003**, *37*, 5337−5347.
(34) Cocker, D. R.; Mader, B. T.; Kalberer, M.; Flagan, R. C.; Seinfeld, J. H. The Effect of Water on Gas−Particle Partitioning of Secondary Organic Aerosol: II. m-Xylene and 1, 3, 5-Trimethylbenzene Photooxidation Systems. *Atmos. Environ.* **2001**, *35*, 6073−6085.
(35) Jang, M. S.; Kamens, R. M. Characterization of Secondary Aerosol from the Photooxidation of Toluene in the Presence of NOx and 1-Propene. *Environ. Sci. Technol.* **2001**, *35*, 3626−3639.
(36) Forstner, H. J. L.; Flagan, R. C.; Seinfeld, J. H. Secondary Organic Aerosol from the Photooxidation of Aromatic Hydrocarbons: Molecular Composition. *Environ. Sci. Technol.* **1997**, *31*, 1345−1358.
(37) Frisch, M. J.; Trucks, G. W.; Schlegel, H. B.; Scuseria, G. E.; Robb, M. A.; Cheeseman, J. R.; Scalmani, G.; Barone, V.; Petersson, G. A.; Nakatsuji, H.et al. *Gaussian 09*, revision A.02; Gaussian, Inc.: Wallingford, CT, 2016.
(38) Chai, J. D.; Head-Gordon, M. Long-range Corrected Hybrid Density Functionals with Damped Atom−Atom Dispersion Corrections. *Phys. Chem. Chem. Phys.* **2008**, *10*, 6615−6620.
(39) Chen, W. L.; Hsieh, C. M.; Yang, L.; Hsu, C. C.; Lin, S. T. A Critical Evaluation on the Performance of COSMO-SAC Models for Vapor−Liquid and Liquid−Liquid Equilibrium Predictions Based on Different Quantum Chemical Calculations. *Ind. Eng. Chem. Res.* **2016**, *55*, 9312−9322.
(40) Singh, D. K.; Rathke, B.; Kiefer, J.; Materny, A. Molecular Structure and Interactions in the Ionic Liquid 1-Ethyl-3-methylimidazolium Trifluoromethanesulfonate. *J. Phys. Chem. A* **2016**, *120*, 6274−6286.
(41) Riplinger, C.; Neese, F. An Efficient and Near Linear Scaling Pair Natural Orbital Based Local Coupled Cluster Method. *J. Chem. Phys.* **2013**, *138*, 034106−034118.
(42) Riplinger, C.; Sandhoefer, B.; Hansen, A.; Neese, F. Natural Triple Excitations in Local Coupled Cluster Calculations with Pair Natural Orbitals. *J. Chem. Phys.* **2013**, *139*, 134101−134113.
(43) Riplinger, C.; Pinski, P.; Becker, U.; Valeev, E. F.; Neese, F. Sparse Maps—A Systematic Infrastructure for Reduced-scaling Electronic Structure Methods. II. Linear Scaling Domain Based Pair Natural Orbital Coupled Cluster Theory. *J. Chem. Phys.* **2016**, *144*, 024109−024120.
(44) Paulechka, E.; Kazakov, A. Efficient DLPNO−CCSD (T)-based Estimation of Formation Enthalpies for C-, H-, O-, and N-Containing Closed-Shell Compounds Validated Against Critically Evaluated Experimental Data. *J. Phys. Chem. A* **2017**, *121*, 4379−4387.

DOI: 10.1021/acs.jpca.9b06331
J. Phys. Chem. A 2019, 123, 9008−9018

(45) Werner, H. −J.; Adler, T. B.; Manby, F. R. General Orbital Invariant MP2-F12 Theory. *J. Chem. Phys.* **2007**, *126*, 164102−164118.
(46) Dunning, T. H. Gaussian Basis Sets for use in Correlated Molecular Calculations. I. The Atoms Boron through Neon and Hydrogen. *J. Chem. Phys.* **1989**, *90*, 1007−1023.
(47) Kendall, R. A.; Dunning, T. H.; Harrison, R. J. Electron Affinities of the Firstrow Atoms Revisited. Systematic Basis Sets and Wave Functions. *J. Chem. Phys.* **1992**, *96*, 6796−6806.
(48) Neese, F. The ORCA Program System. *Wiley Interdiscip. Rev.: Comput. Mol. Sci.* **2012**, *2*, 73−78.
(49) Jensen, F. *Introduction to Computational Chemistry*; John Wiley & Sons, 2017.
(50) Vereecken, L.; Francisco, J. S. Theoretical Studies of Atmospheric Reaction Mechanisms in the Troposphere. *Chem. Soc. Rev.* **2012**, *41*, 6259−6293.
(51) Fukui, K. The Path of Chemical-Reactions—The IRC Approach. *Acc. Chem. Res.* **1981**, *14*, 363−368.
(52) Hratchian, H. P.; Schlegel, H. B. *Theory and Applications of Computational Chemistry: The First 40 Years*; Elsevier: Amsterdam, 2005; pp 195−249.
(53) Zhang, J.; Dolg, M. ABCluster: The Artificial Bee Colony Algorithm for Cluster Global Optimization. *Phys. Chem. Chem. Phys.* **2015**, *17*, 24173−24181.
(54) Zhang, J.; Dolg, M. Global Optimization of Clusters of Rigid Molecules by the Artificial Bee Colony Algorithm. *Phys. Chem. Chem. Phys.* **2016**, *18*, 3003−3010.
(55) Bannwarth, C.; Ehlert, S.; Grimme, S. GFN2-xTB—An Accurate and Broadly Parametrized Self-Consistent Tight-Binding Quantum Chemical Method with Multipole Electrostatics and Density-Dependent Dispersion Contributions. *J. Chem. Theory Comput.* **2018**, *15*, 1652−1671.
(56) Grimme, S.; Bannwarth, C.; Shushkov, P. A Robust and Accurate Tight-Binding Quantum Chemical Method for Structures, Vibrational Frequencies, and Noncovalent Interactions of Large Molecular Systems Parametrized for All spd-Block Elements (Z = 1−86). *J. Comput. Theory Chem.* **2017**, *13*, 1989−2009.
(57) Matsuki, A.; Schwarzenboeck, A.; Venzac, H.; Laj, P.; Crumeyrolle, S.; Gomes, L. Cloud Processing of Mineral Dust: Direct Comparison of Cloud Residual and Clear Sky Particles during AMMA Aircraft Campaign in Summer 2006. *Atmos. Chem. Phys.* **2010**, *10*, 1057−1069.
(58) Pöschl, U. Atmospheric Aerosols: Composition, Transformation, Climate and Health Effects. *Angew. Chem., Int. Ed.* **2005**, *44*, 7520−7540.
(59) Li, W. J.; Shao, L. Y. Observation of Nitrate Coatings on Atmospheric Mineral Dust Particles. *Atmos. Chem. Phys.* **2009**, *9*, 1863−1871.
(60) Marsden, N. A.; Ullrich, R.; Möhler, O.; Eriksen Hammer, S.; Kandler, K.; Cui, Z.; Williams, P. I.; Flynn, M. J.; Liu, D.; Allan, J. D.; et al. Mineralogy and Mixing State of North African Mineral Dust by On-Line Single-Particle Mass Spectrometry. *Atmos. Chem. Phys.* **2018**, *19*, 2259−2281.
(61) Claquin, T.; Schulz, M.; Balkanski, Y. J. Modeling the Mineralogy of Atmospheric Dust Sources. *J. Geophys. Res.* **1999**, *104*, 22243−22256.
(62) Ji, Y.; Wang, H.; Li, G.; An, T. Theoretical Investigation on the Role of Mineral Dust Aerosol in Atmospheric Reaction: A Case of the Heterogeneous Reaction of Formaldehyde with NO_2 onto SiO_2 Dust Surface. *Atmos. Environ.* **2015**, *103*, 207−214.
(63) Moreno, T.; Querol, X.; Castillo, S.; Alastuey, A.; Cuevas, E.; Herrmann, L.; Mounkaila, M.; Elvira, J.; Gibbons, W. Geochemical Variations in Aeolian Mineral Particles from the Sahara−Sahel Dust Corridor. *Chemosphere* **2006**, *65*, 261−270.
(64) Lindberg, J. D. The Composition and Optical Absorption Coefficient of Atmospheric Particulate Matter. *Opt. Quant. Electron.* **1975**, *7*, 131−139.
(65) Krueger, B. J.; Grassian, V. H.; Cowin, J. P.; Laskin, A. Heterogeneous Chemistry of Individual Mineral Dust Particles from Different Dust Source Regions: The Importance of Particle Mineralogy. *Atmos. Environ.* **2004**, *38*, 6253−6261.
(66) Adushkin, V. V.; Chen, B. B.; Popel, S. I.; Dubinskii, A. Y.; Weidler, P. G.; Friedrich, F. Experimental Study of Small-Scale Mineral Particles in the Atmosphere of Central Asia. *Izv. Phys. Solid Earth* **2018**, *54*, 330−335.
(67) Zeb, B.; Alam, K.; Sorooshian, A.; Blaschke, T.; Ahmad, I.; Shahid, I. On the Morphology and Composition of Particulate Matter in an Urban Environment. *Aerosol Air Qual. Res.* **2018**, *18*, 1431−1447.
(68) Kandler, K.; Schütz, L.; Deutscher, C.; Ebert, M.; Hofmann, H.; Jäckel, S.; Jaenicke, R.; Knippertz, P.; Lieke, K.; Massling, A.; et al. A. Size Distribution, Mass Concentration, Chemical and Mineralogical Composition and Derived Optical Parameters of the Boundary Layer Aerosol at Tinfou, Morocco, during SAMUM 2006. *Tellus B* **2009**, *61*, 32−50.
(69) Kumar, A.; Marcolli, C.; Luo, B.; Peter, T. Ice Nucleation Activity of Silicates and Aluminosilicates in Pure Water and Aqueous Solutions−Part 1: The K-Feldspar Microcline. *Atmos. Chem. Phys.* **2018**, *18*, 7057−7079.
(70) Ryder, C. L.; Marenco, F.; Brooke, J. K.; Estelles, V.; Cotton, R.; Formenti, P.; McQuaid, J. B.; Price, H. C.; Liu, D.; Ausset, P.; Rosenberg, P. D.; et al. Coarse-Mode Mineral Dust Size Distributions, Composition and Optical Properties from AER-D Aircraft Measurements over the Tropical Eastern Atlantic. *Atmos. Chem. Phys.* **2018**, *18*, 17225−17257.
(71) Civalleri, B.; Garrone, E.; Ugliengo, P. Vibrational Modes of Isolated Hydroxyls of Silica Computed Ab Initio in a Cluster Approach. *Chem. Phys. Lett.* **1998**, *294*, 103−108.
(72) Iuga, C.; Vivier-Bunge, A.; Hernandez-Laguna, A.; Sainz-Diaz, C. I. Quantum Chemistry and Computational Kinetics of the Reaction between OH Radicals and Formaldehyde Adsorbed on Small Silica Aerosol Models. *J. Phys. Chem. C* **2008**, *112*, 4590−4600.
(73) Pereira, J. C. G.; Catlow, C. R. A.; Price, G. D. Ab Initio Studies of Silica-Based Clusters. Part II. Structures and Energies of Complex Clusters. *J. Phys. Chem. A* **1999**, *103*, 3268−3284.
(74) Hermans, I.; Vereecken, L.; Jacobs, P. A.; Peeters, J. Mechanism of the Catalytic Oxidation of Hydrocarbons by N-hydroxyphthalimide: A Theoretical Study. *Chem. Commun.* **2004**, *9*, 1140−1141.
(75) Eckart, C. The Penetration of a Potential Barrier by Electrons. *Phys. Rev.* **1930**, *35*, 1303−1309.
(76) Sarkar, S.; Mallick, S.; Kumar, P.; Bandyopadhyay, B. Isomerization of Methoxy Radical in the Troposphere: Competition between Acidic, Neutral and Basic Catalysts. *Phys. Chem. Chem. Phys.* **2017**, *19*, 27848−27858.
(77) Wehner, B.; Wiedensohler, A.; Tuch, T. M.; Wu, Z. J.; Hu, M.; Slanina, J.; Kiang, C. S. Variability of the Aerosol Number Size Distribution in Beijing, China: New Particle Formation, Dust Storms, and High Continental Background. *Geophys. Res. Lett.* **2004**, *31*, L22108−L22111.
(78) Möhler, O.; Field, P. R.; Connolly, P.; Benz, S.; Saathoff, H.; Schnaiter, M.; Wagner, R.; Cotton, R.; Krämer, M.; Mangold, A.; Heymsfield, A. J. Efficiency of the Deposition Mode Ice Nucleation on Mineral Dust Particles. *Atmos. Chem. Phys.* **2006**, *6*, 3007−3021.
(79) Karagulian, F.; Santschi, C.; Rossi, M. J. The Heterogeneous Chemical Kinetics of N_2O_5 on $CaCO_3$ and Other Atmospheric Mineral Dust Surrogates. *Atmos. Chem. Phys.* **2006**, *6*, 1373−1388.
(80) Gao, Z.; Wang, X.; Shen, L.; Xiang, H.; Wang, H. Characteristics of Aerosol Chemical Compositions and Size Distributions during a Long-Range Dust Transport Episode in an Urban City in the Yangtze River Delta. *Atmosphere* **2019**, *10*, 68−82.
(81) *Chemcraft-Graphical Software for Visualization of Quantum Chemistry Computations*, 2010. https://www.chemcraftprog.com.
(82) Sipilä, M.; Berndt, T.; Petäjä, T.; Brus, D.; Vanhanen, J.; Stratmann, F.; Patokoski, J.; Mauldin, R. L.; Hyvärinen, A. P.; Lihavainen, H.; et al. The Role of Sulfuric Acid in Atmospheric Nucleation. *Science* **2010**, *327*, 1243−1246.

DOI: 10.1021/acs.jpca.9b06331
J. Phys. Chem. A 2019, 123, 9008−9018